Aerodynamic Flow Control of a Channel Wing

Bojan Vukasinovic [1], Michael DeSalvo[2], Robert B. Funk [3], and Ari Glezer[4]

[1,2,4]*Woodruff School of Mechanical Engineering,*
Georgia Institute of Technology, Atlanta, GA 30332-0405

[3]*Georgia Tech Research Institute ATAS, Smyrna, GA 30080*

Abstract

Aerodynamic flow control of a channel wing model using fluidic actuation was investigated in wind tunnel experiments. Trailing edge circulation control (CC) for enhancement of short takeoff and landing (STOL) was effected using independent arrays of fluidically oscillating jet actuators over integrated Coanda surfaces along the trailing edges of the wing's outer span segment (upstream of a 70° flap) and of the channel. Aerodynamic distributed bleed (ADB) actuation through a spanwise segment near mid-chord was used for regulation of aerodynamic loading for improved maneuverability at both takeoff/landing and in-flight conditions. In addition, fluidically oscillating jets were also used along the leading edge for suppression of stall. The effectiveness of the fluidic actuation for CC was assessed in the absence and presence of power to the channel propeller drive over a range of thrust coefficients $0 < C_T < 0.6$. The present measurements demonstrated that at a dynamic pressure of 96 Pa for $0° < \alpha < 8°$, the CC lift increments induced by the outer wing and channel actuators arrays are additive, yielding $\Delta C_L/\Delta C_D \approx 7 - 10$ at $C_T = 0.6$. In addition, at $\alpha = 8°$, use of CC at $C_T = 0$ leads to a 43% reduction in dynamic pressure required to achieve takeoff lift. At the takeoff speed achieved using full CC and propeller thrust, the base wing lift accounts for 45% of the total lift, the propeller in the channel for 15%, trailing-edge flow control in the channel for 12% and trailing-edge flow control on the outer wing panel for the remaining 28%. These improvements in STOL characteristics were extended into post-stall conditions using the leading-edge actuation, albeit at somewhat reduced efficiency.

I. Introduction

In a unique high-lift concept introduced by Custer (1929), an aircraft wing was modified to include a channel section near its root that partially enclosed the engine and propeller from below. The flow driven by the propeller over the inner surface of the channel engenders lift even in the absence of aircraft motion, and augmented by the contribution of the vertical component of the thrust can enable aircraft to take off and sustain flight thereafter at low speed. This concept attracted significant interest and led to full-scale NACA tests (Pasamanick, 1953) that were followed by analysis by Blick and Homer (1971). Although several channel wing aircraft configurations were successfully demonstrated in the following years, the up-and-away and engine-out performance

---

[1] Research Engineer, AIAA Member.
[2] Research Engineer, AIAA Member.
[3] Research Engineer, AIAA Associate Fellow.
[4] Professor, AIAA Fellow.

(Gunther et al. 2000) hindered its commercial adoption. However, recent interest in short take-off and landing (STOL) performance brought about by the rapid expansion of unmanned aerial vehicles (UAVs) and urban mobility needs (Keane and Keane, 2016, Mihalik and Keane, 2022) has led to renewed interest in channel wings (Zilberman et al., 2021).

High lift on conventional wings was implemented using simple airfoil slots as early as the 1930s (Haus, 1931) and was later augmented in the 1950s by using integrated 2-D high-speed wall-bounded or free jets issuing either tangent to a flap or at the trailing edge of the airfoil at some fixed angle (e.g., Davidson 1956, Dimmock 1957, Williams et al. 1961). The modification of the embedding flow over the airfoil by the presence of the jet (or 'jet flap' as it was called) led to a lift increment larger than the vertical component of the jet thrust. More advanced aerodynamic circulation control evolved from the jet flap approach by exploiting the Coanda effect associated with a 2-D wall jet issuing over a curved airfoil trailing edge or flap surface (e.g., Englar 1996, 2000, 2005). The presence of the jet delays flow separation over the curved surface, with the extent of the attached flow increasing with jet momentum coefficient and the attachment over the Coanda surface leading to partial vectoring of the flow over the surface. The interaction of the actuation or control jet and the cross flow leads to alterations in the global flow, including the location of the trailing edge stagnation point. It is noteworthy that Englar and Campbell (2002) demonstrated that the high lift performance of a channel wing with propeller thrust (i.e., powered) can be further enhanced using circulation control effected by a continuous 2-D jet blowing over a Coanda surface at the trailing edge of the channel that can lead to lift coefficients up to $C_L = 9$, albeit with significant actuation momentum coefficients.

Aerodynamic performance of conventional wings can be enhanced by using distributed bleed actuation without the need for a dedicated air source. The bleed flow is driven across the wing through openings in the surface by pressure differences between the pressure and suction surfaces and regulated by low power louvers integrated into the surface. Lifting surfaces with passive bleed have been investigated since the 1920s (e.g., Lachmann, 1924), and bleed has been demonstrated in applications including reduction of bluff body base drag (Tanner, 1975), separation control (Kraushaar and Chokani 1997), and limited control of aerodynamic loads (Hu et al., 2014). The investigations of Kearney and Glezer (2011, 2013, 2014) showed that interaction between a controlled bleed flow and the adjacent cross flow can be tailored to leverage the generation and regulation of vorticity concentrations on or near the surface, resulting in significant alteration of the flow and thereby the aerodynamic loads. Below stall, quasi-steady bleed actuation can lead to a significant lift reduction (up to 88%, e.g. at $\alpha = 0°$) that, depending on the bleed configuration, can be accompanied either by drag decrease (up to -27% at $\alpha = 8°$) or increase (up to +125% at $\alpha = 4°$). The bleed flow through the openings can be regulated using low-power louvers, enabling the aerodynamic loads to be continuously varied on time scales significantly faster than for motion of conventional control surfaces, and the size and location of the openings can be adjusted to vary the changes in aerodynamic loads. More recently, DeSalvo et al. (2019) utilized distributed air bleed to fluidically alter the aerodynamic loads on a 3-D wing in a high-lift configuration. Bleed at flap angle $\theta = 24°$ results in lift reduction and changes in rolling moment C_R (maximum $\Delta C_R / C_{R0} = -0.29$ at $\alpha = 0°$).

Design studies in the DARPA CRANE program investigated various concepts where application of active flow control provides a significant performance advantage. The channel wing with active flow control for STOL was identified as the most promising candidate, a conceptual design was produced, and a subscale wind tunnel model was constructed and tested. In the present

investigations, aerodynamic flow control was incorporated into the channel wing model for enhancement of short takeoff and landing (STOL) performance and for regulation of aerodynamic loads for improved maneuverability. Circulation control at low angles of attack up to near-stall conditions is effected at the trailing edge of the channel and over outboard flaps using spanwise-segmented unsteady arrays of fluidically-oscillating wall jets based on the earlier investigations of Vukasinovic et al. (2023), with additional fluidically-oscillating wall jet arrays installed near the leading edge of the suction surface to mitigate separation at high angles of attack. Aerodynamic bleed in various configurations is investigated based on earlier investigations by DeSalvo et al. (2021) to vary aerodynamic loads for improved maneuverability.

II. Experimental Setup and Procedures

The present experiments were conducted in the John J. Harper 7 × 9 ft. (2.1 × 2.7 m) Wind Tunnel, a closed circuit atmospheric wind tunnel at Georgia Tech (maximum speed 50 m/s, turbulence level up to 0.3%). The test section is equipped with a floor-mounted force balance and turntable system for varying the model's angle of attack. The channel wing model is built on a ladder frame consisting of two spanwise spars anchored in tandem by chordwise spacers.

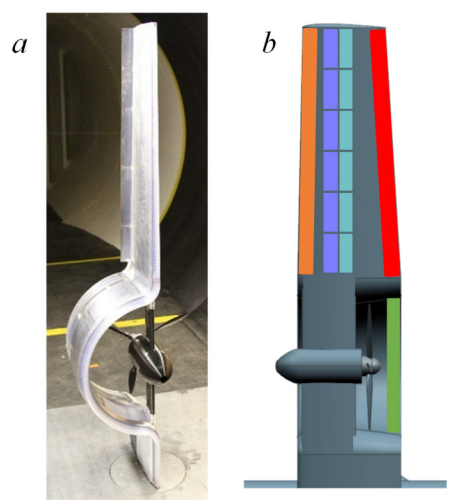

Figure 1. *a) The channel wing model installed in the wind tunnel; and b) Schematics rendition of the arrays of fluidically-oscillating jet actuators along the trailing edges of the* ***channel*** *and the* ***wing's outboard section*** *and of the* ***wing's leading edge.*** *Each of the* ***upstream*** *and* ***downstream*** *rows of segmented bleed ports on the wing's outboard section have an open area* $\Phi = 3.5\%$ *and are operated in several spanwise and streamwise configurations.*

Figure 1a shows an upstream view of the model installed in the wind tunnel test section on a rotational stage that protrudes through an elevated ground plane above the test section floor to reduce the effects of the wall boundary layer. The channel wing model, based on an NACA 64A214 airfoil, has a span of 1.68 m with a 0.51m diameter channel extending from $0.149 < z/s < 0.45$. The outboard section of the wing (0.924 m span) is tapered (leading edge 1.16°, trailing edge -3.53°) such that the chords at the channel and the wingtip were 0.354 m and 0.283 m, respectively, yielding $\bar{c} = 0.318\,m$. The aerodynamic loads on the model are measured using a combination of a 6-DOF force sensor and two single axis load cells.

The propulsion flow through the channel is driven by a three-bladed propeller attached to a *Hacker* Q80 electric motor mounted on a support strut as shown in Figure 1a and controlled by a *Jeti* electronic speed controller from the laboratory computer. The propulsion thrust was characterized on a separate vertical test stand in the wind tunnel over a range of tunnel speeds and motor RPM (the drag of the test stand and nacelle were measured in the absence of the propeller to correct the measured thrust). The propeller was characterized at its final trimmed size (0.50 m diameter) required to fit in the channel but is still referred to by its original size (i.e., 20×14, 20" diameter, 14" pitch). The thrust and torque coefficients C_T and C_Q were computed based on the tunnel speed and an advance ratio (tunnel speed/tip speed) as shown in Figure 2. The advance ratio was used with a calibration equation developed from the isolated testing to calculate C_T during the channel wing testing.

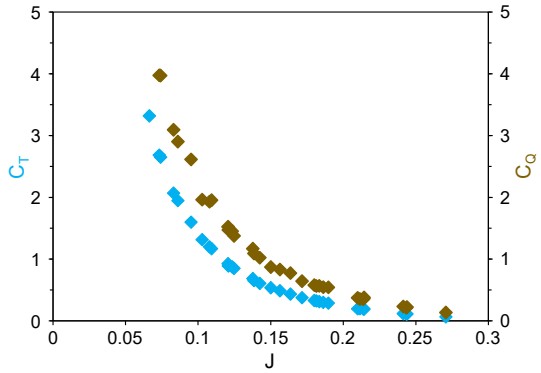

Figure 2. *The thrust and torque coefficients with the advance ratio, measured for the isolated propeller.*

The layout of the pneumatic and bleed fluidic actuator arrays is shown schematically in Figure 1b using color-coded renditions. The leading and trailing edge segments of the outboard section of the wing and the trailing edge of the channel contain monolithic integrated arrays of fluidically oscillating wall jet actuators and their ancillary pneumatic plumbing that were fabricated using stereolithography (the leading-edge actuators were used for suppression of stall that hinders the trailing edge CC, when needed). The leading-edge actuator orifices present a boundary layer trip whether operating or not and provide turbulent flow over the wing and channel to limit any transition effects. The oscillating actuator jets are equally spaced and issue from orifices measuring $0.0031\bar{c} \times 0.0047\bar{c}$. The trailing edge actuators on the outboard section of the wing are integrated upstream of a $0.1c$ flap deflected at $\theta = 70°$ relative to the chord while the trailing edge actuators in the channel were coupled to a half-round Coanda surface ($0.024\bar{c}$ diameter) for bi-directional control. In the present model, the outboard leading edge and trailing edge, and channel trailing edge fluidic actuator arrays are independently operated. The operating condition of the actuators is characterized using the actuation mass flow rate and global momentum coefficients $C_q = \dot{m}/(\rho_o \cdot U_o \cdot A_p)$ and $C_\mu = T/(q \cdot S)$, respectively, where $\dot{m}$ and T are the (measured) global actuation mass flow rate and thrust.

Various distributed bleed actuation configurations are realized by forming the outer aerodynamic surface of the wing model from a set of replaceable skin segments containing openings for bleed flow, which are fabricated by rapid prototyping and attached to an internal support structure as shown schematically in Figure 1b. The bleed openings consist of arrays of rectangular slots (12 mm spanwise by 3.7 mm chordwise) on the pressure and suction surfaces that are covered in thin adhesive film when not in use. In the primary tests (cf. §IV), two chordwise arrays spanning the full outer segment of the model (Figure 1b) are tested separately (each having an open area $\Phi \approx 3.5\%$ of model reference area) and together ($\Phi \approx 6.9\%$). In addition, tests are conducted in which bleed from both chordwise arrays operated together is selectively issued from six equally-sized spanwise segments ($\Phi \approx 1.2\%$ each) between the channel and the wingtip.

III. Circulation Control

III.A. Characterization of the Flow Control Elements

Arrays of flow control elements utilized along the trailing edge of the model were developed from fluidically-oscillating jet arrays tested on a 2-D wing (labeled as C3D-1 by Vukasinovic, Glezer, and Funk, 2023), while the wing leading edge array was adopted from the 2-D wing studies by DeSalvo and Glezer (2023). Prior to manufacturing the full-scale model flow control segments, small subsections of the fully-designed flow control modules at the trailing edges were manufactured for bench test characterization of the jets' thrust generation relative to the supplied mass flow rate. In addition, results of the earlier characterization of the trailing edge flow control array for the 2-D airfoil Coanda-assisted flow control are included in Figure 3 for reference. Figure 3a shows the corresponding results in terms of the momentum coefficient generated by a single

jet. Although these measurements were made in the absence of cross flow, to put these results in a context of the wind tunnel test, they are scaled by the default wind tunnel dynamic pressure q and the model planform area A. If considered relative to the dimensionless supply flow rate of the jet (Figure 3a), the test results suggest that each of these three flow control modules at both the flap and Coanda trailing edges generates different total thrust per active control jet. Clearly, a measure of the supply flow rate is important as one of the critical dimensional parameters for the control input. However, the resulting jet mass flow rate is highly dependent on the total losses, both in the supply system and across the flow control elements. Since the control elements are designed to be the same, it can be assumed that once the supply line losses are excluded from consideration, the individual jet performances should be similar. This is verified by plotting the jet total thrust as a function of the jet plenum supply pressure in Figure 3b, ensuring the same pressure drop across individual flow control elements in all the three modules. As also recently argued by Oshima et al. (2023), this represents a better, energy-based basis for the flow control device comparison. As seen in Figure 3b, the generated thrust of each jet is reasonably close relative to the pressure difference, which is even more significant due to the different Coanda extensions for each of the three modules, where one of them even extends into a flap. These results also point to a need of careful consideration for the minimization of pressure losses for improved efficiency of the flow control devices.

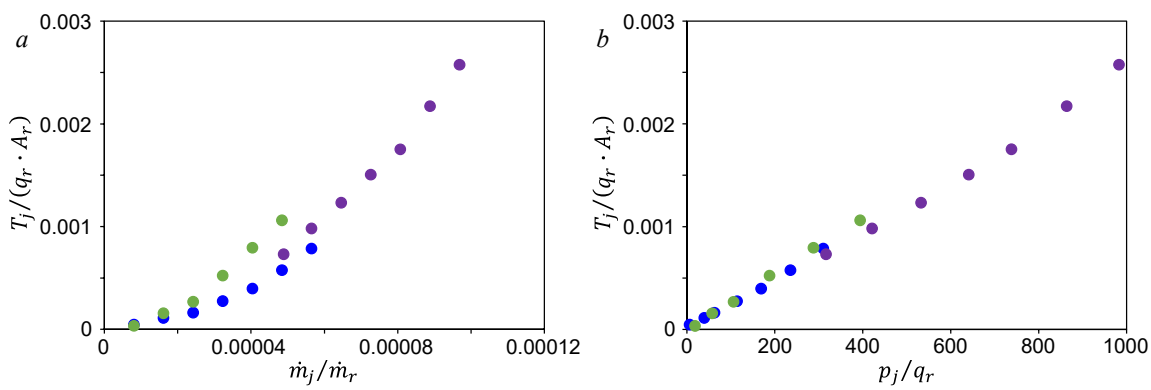

Figure 3. *Bench calibration of the jet thrust T_j relative to its flow rate (a) and pressure (b) for the trailing edge wing (●) and channel (●) control modules, relative to the reference test dynamic pressure q_r and the model planform area A_r. For reference, the corresponding jet trust for circulation control (●) by Vukasinovic, Glezer, and Funk (2023) is overlaid in each plot.*

After the wind tunnel model was fully assembled, and prior to any flow control studies, the full banks of control arrays were characterized in a similar manner as on the bench (cf. Figure 3). Just as in Figure 3, the resulting measured total thrust by each of the flow control modules is shown in Figure 4a relative to the default free stream dynamic pressure and planform area, although these measurements are done in the absence of flow. It is interesting to note that the total thrust generated by the leading-edge wing flow control array and that along the trailing edge of the channel are nearly identical for a given total mass flow rate input to the arrays. Clearly, this is not the case along the wing trailing edge, where a significantly higher population of jets considerably reduces a jet-generated thrust for a given supply mass flow rate. Still, there is an important distinction for this array, as it acts over an aggressive flap, which significantly assists the jets' flow control effect. Lastly, even when the generated thrusts are compared relative to individual jets (Figure 4b), the relationship among the control elements in different control modules remains unchanged: the channel and the wing leading edge jets generate about the same unit thrust, while

the trailing wing jets still generate a lower thrust per jet, although the reduction relative to the other two is smaller than when the total thrusts were compared (cf. Figure 4a). This difference clearly points one more time to the significance of the pressure losses on the flow control thrust delivery, and raises the importance of their minimization during the design process. Still, the internal conduits supplying air along the full outer wing are inherently more complex.

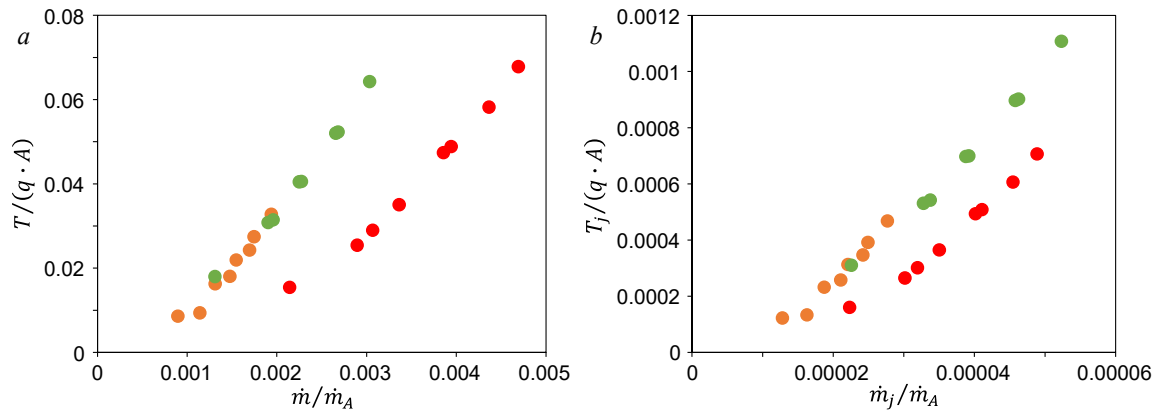

Figure 4. *Total (a) and the thrust generated by a single flow control jet (b) in the absence of cross flow with the total (a) and individual (b) supply mass flow rate for the trailing edge wing (●) and channel (●), and the wing leading edge (●) control modules, relative to the default test dynamic pressure q and the model planform area A.*

III.B. Implementation of Circulation Control

Although the main interest in flow control-enhanced circulation about a channel wing is related to the propelled flow through the wing channel, it is informative to assess the flow control capabilities with the propeller inactive, which would also represent a prop-out condition. Figure 5 first indicates capabilities of the flow control over the outer wing section under the condition of the

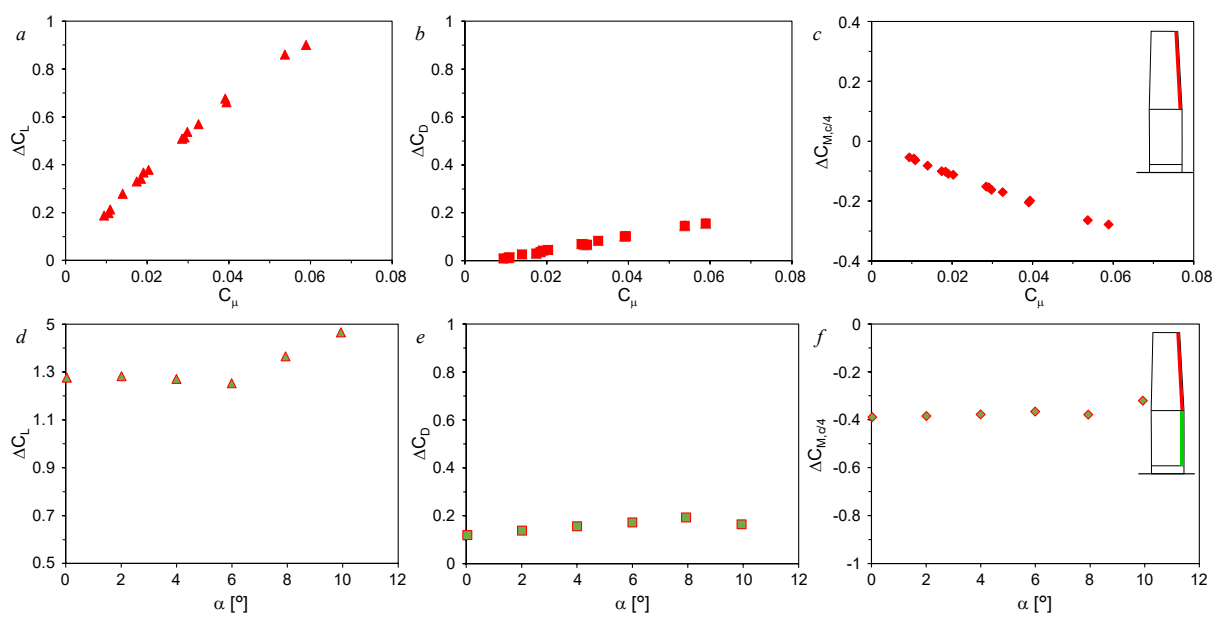

Figure 5. *Incremental change in lift (a,d), drag (b,e), and pitch (c,f) coefficients ($C_T = 0$) with the wing trailing edge flow control momentum coefficient for angle of attack $\alpha = 0°$ (a–c), and with the angle of attack for the trailing edge $C_\mu = 0.11$ (d–f).*

least generated lift – at zero angle of attack (Figures 5a–c). All control-induced aerodynamic loads are shown as increments relative to the base flow with the propeller inactive, over a range of the total jet momentum coefficient of all active jets along the wing trailing edge (inset schematics in Figure 5c). Lift coefficient increment increases in a nearly-linear fashion with C_μ (Figure 5a), reaching $\Delta C_L \approx 0.9$ at $C_\mu \approx 0.06$. As expected, the lift-induced drag component also increases progressively with C_μ (Figure 5b), yielding $\Delta C_L/\Delta C_D \approx 6$ for the highest measured lift increment. Lastly, the pitching moment $C_{M,c/4}$, calculated with respect to the quarter-chord point on the main wing chord line, where the variation of pitching moment with α is minimal (below stall), becomes increasingly negative (nose-down) as C_μ is increased (Figure 5c), pointing to the need for a commensurate increase in the countering moment for maintaining trimmed flight. In addition to the C_μ-variation, another assessment is done to test the flow control sensitivity to angle of attack, for $C_\mu = 0.11$ and the flow control applied across the full trailing edge (inset in Figure 5f). In principle, both forces and the pitch moment (Figures 5d–f) indicate a fairly consistent flow control effect across all the pre-stall angles, except a small uptick in the lift coefficient increment with the approach to stall (Figure 5d). In addition, as the flow control is applied on both channel and wing trailing edge, an increased $\Delta C_L/\Delta C_D \approx 7 - 10$ is measured over these pre-stall angles of attack.

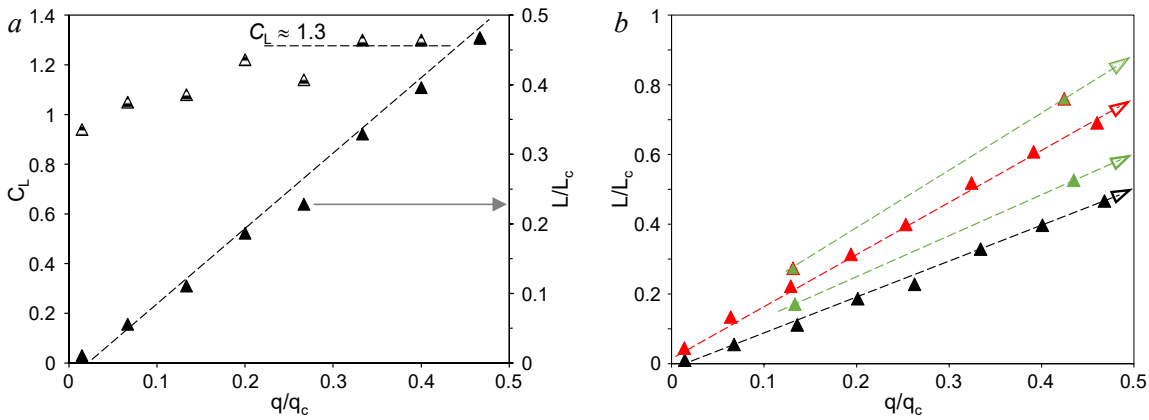

Figure 6. *Baseline lift/lift coefficient (▲) with the free stream dynamic pressure q for $\alpha = 8°$ and $C_T = 0$ (a), and the resulting lift for the flow controlled at the channel (▲) and at the wing (▲) trailing edge, and at both trailing edges simultaneously (▲, red border).*

One of the critical parameters for the circulation control assessment is related to its improved short takeoff and landing (STOL) characteristics. To facilitate such assessment in the present investigation, takeoff lift for a conceptual channel wing platform was determined at the wind tunnel model scale and the takeoff lift per wing $L_c = 500$ N compared to the measured lift in the wind tunnel experiments. In the absence of the prop and with the flow control arrays inactive, the highest pre-stall angle of attack ($\alpha = 8°$) would generate the maximum attainable lift ($C_L \approx 1.3$, cf. Figure 10a), and the free stream speed in the test section was varied such that its dynamic pressure was changed from $q/q_c = 0.07 - 0.47$, in equal increments. The resulting aerodynamic lift and lift coefficients are shown in Figure 6a. The dynamic pressure is normalized by the dynamic pressure (q_c) required to achieve L_c at the baseline condition. It appears that C_L still has some Reynolds-number dependence at lower speeds, but it reaches saturation at approximately $C_L = 1.31$, while the dimensional lift only attains less than half that needed for takeoff ($L/L_c \approx 0.47$). This condition assumes the no-prop channel wing operation, which is used here only to provide the upper q limit, as a reference point for the prop-off, no-AFC scenario.

In addition to the no-AFC flow characterization shown in Figure 6a, effectiveness of the individual channel and wing trailing-edge actuations, as well as simultaneous actuation by both flow control arrays was tested over a range of the flow control parameters (C_μ). Figure 6b indicates only the highest achieved lift enhancement from each of these flow control configurations, where the data points are color-coded in accord with the corresponding flow control arrays that are utilized. The trailing-edge wing flow control is more effective than the trailing-edge channel in overall effect, although this is a consequence of the disproportional total spatial coverage of the two flow control arrays, which largely favors the wing AFC array, consisting of ~65% more flow control elements than the channel trailing edge. Another important observation is that the effect of concomitant actuation using both flow control arrays corresponds to the sum of the effects of actuation using each array individually, which points to no significant interference between the separate flow control interactions over the inner surface of the channel and over the outboard wing section. Using similar extrapolation done for q_c, if the measured trends with q in Figure 6b are extrapolated, as marked by arrows, up to the L_c that is deemed needed for takeoff, a significant reduction of the needed speed, through the proxy of q, is obtained: individual channel and individual wing flow control reduces the needed q to $0.83q_c$ and $0.67q_c$, respectively, while both trailing-edge of flow control arrays combined further reduce the needed q to $0.57q_c$.

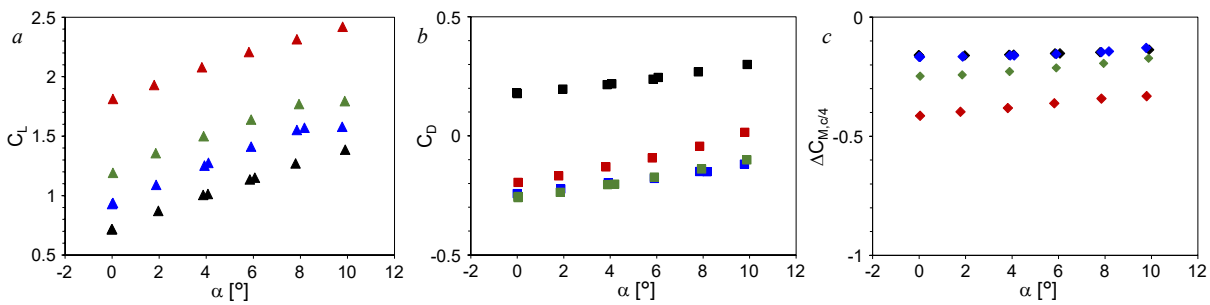

Figure 7. *Lift (a), drag (b), and pitch (c) coefficients with angle of attack for the base (black) flow for $q = 0.46q_c$, and the prop-assisted flow ($C_T = 0.41$) without flow control (blue) and with the channel ($C_\mu = 0.035$, green) and both the channel and wing ($C_\mu = 0.068$, red) trailing edge flow control.*

Certainly, the most important aspect of the circulation control of a channel wing includes the prop-operating wing configuration. As with the non-prop assessment, different flow configurations are tested across a range of pre-stall angles ($q/q_c = 0.46$), having the base, no-prop case as a reference, followed by the successive addition of the prop, channel, and the outer wing flow control. Figure 7 shows the resulting changes in the aerodynamic loads, similar to the assessment of the no-prop cases (cf. Figure 5). Every lift coefficient trend shows nearly linear dependence on the angle of attack, except a drop at the highest angle that is already within the incipient flow separation domain (Figure 7a). The highest attained base flow lift coefficient, just above $C_L = 1.3$, increases by ~30% when the prop is activated ($C_T = 0.41$). When the channel trailing edge flow control is effected ($C_\mu = 0.035$), C_L increases by ~50%. Finally, when the wing trailing edge flow control is added, with total $C_\mu = 0.068$, there is the most substantial increase in the lift coefficient, which reaches nearly $C_L = 2.5$ at the highest angle of attack. Activation of the prop clearly has a dramatic consequence on the base flow drag (Figure 7b), as the thrust coefficient is higher than the aerodynamic base drag, thus inducing a net thrust. It is interesting that activation of the channel flow control has very little effect on this net thrust, which was already noted in prior work (Vukasinovic, Glezer and Funk, 2023) where circulation control was effected by a discrete array of flow control jets over a rounded Coanda surface, as along the trailing edge of the channel.

Contrary to this case, when the circulation control is activated over the flap as well, a rather typical lift-induced-drag relationship is recovered with respect to drag. Still, even at the highest lift gain ($C_L \approx 2.5$), the net drag remains nearly zero due to the thrust contribution by the prop. Lastly, each component added to the base flow pitch moment (Figure 7c) only further reinforces the same moment sense, while preserving the weak positive gradient that appears to level towards the stall, so that the controlled flow characteristics remain unchanged from the standpoint of the pitch stability in the pre-stall region.

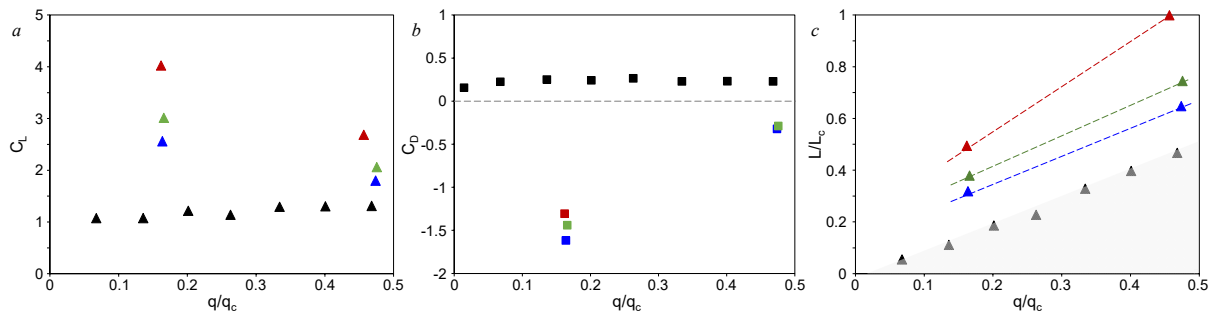

Figure 8. *Attained lift (a) and drag (b) coefficients, and the relative lift (c) with q for the flow assisted by the prop only (blue), and controlled by the channel (green) and simultaneous wing and channel (red) AFC, at $\alpha = 8°$. Base flow (black) is shown for reference.*

STOL characteristics of the prop-operated channel wing with circulation control are summarized in Figure 8, in a similar fashion as in the absence of prop (Figure 6). Figures 8a and b illustrate the main results in terms of the lift and drag coefficients under the same conditions considered without the prop, at the angle of attack $\alpha = 8°$, and for the characteristic dynamic pressures $q/q_c = 0.17$ and 0.47. The base lift and drag are also included in the plots, for reference, over the full sweep of the free stream dynamic pressures $q/q_c = 0.07 – 0.47$. While both the lift and drag coefficient of the base flow only weakly depend on q, as can be expected, effects of the added prop strongly depend on q, inducing much larger force coefficients at lower q. Thus, the prop-assisted lift and drag coefficients at $q/q_c = 0.17$ reach $C_L \approx 2.5$ and $C_D \approx -1.6$ (net thrust), while at $q/q_c = 0.47$, the resulting coefficients are $C_L \approx 1.8$ and $C_D \approx -0.3$. Similarly, activation of the circulation control over the channel trailing edge and along the full trailing edge (channel and the wing) induces larger increments in the force coefficients at lower q. It is noted that the maximum C_L reaches ~4 at $q/q_c = 0.17$. The drag penalty is also stronger at lower q, where each activation of the flow control arrays somewhat reduces the net thrust induced by the prop. When considering the takeoff conditions, it is more informative to express the net attained lift force, relative to the lift force needed for takeoff, as shown in Figure 8c for the same data shown in Figure 8a. Similar to the analysis in Figure 6, attained lift forces are expressed as fractions of the takeoff lift force L_c, and the dynamic pressure needed for takeoff (a proxy for the speed) is estimated by extrapolation of the measured data up to $L/L_c = 1$. Thereby, it is estimated that the prop operation would reduce the required takeoff dynamic pressure to $0.8q_c$, while activation of the channel circulation control would further reduce the needed q to $0.7q_c$. Finally, when both the channel and wing circulation control are active, there is no need to extrapolate the measurements, as the takeoff condition is reached in the wind tunnel tests (see Figure 8c) at $0.45q_c$, i.e., less than half the dynamic pressure of the base wing geometry. This indicates a need to accelerate to a lower speed to achieve takeoff lift resulting a shorter takeoff run. Takeoff field length is proportional to wing loading and inversely proportional to the product of $C_{L,max,TO}$ and thrust/weight. For the present case, with constant wing loading and thrust/weight, the takeoff field length (TOFL) would be inversely

proportional to $C_{L,max}$. Using the wing alone as a reference, the TOFL would be reduced by 23.5% due to the prop effect in the channel, 35% when adding AFC in the channel and 50% when adding AFC on the outer wing panel.

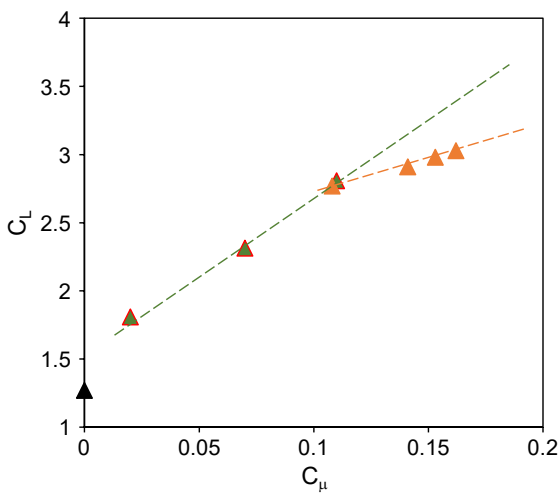

Figure 9. *Lift coefficient with the total flow control momentum coefficient for the base flow at α = 8° and q = 0.27q_c (▲), and the pre-stall flow control along the trailing edge (▲) and the past-stall flow control assisted by the wing leading edge separation control (▲).*

Although not utilized up to this point, the channel wing model is equipped with a wing leading edge flow control array for management of leading-edge separation upon approaching stall. This additional flow control array is intended to test extension of the pre-stall circulation control to higher angles of attack, where leading-edge flow control is needed to maintain attached flow over the suction surface in order to ensure effectiveness of the trailing edge circulation control as in the pre-stall conditions. Figure 9 illustrates such effects of the leading-edge flow control at $\alpha = 8°$ and for $q/q_c = 0.27$. Prior to flow control activation (C_μ = 0), the flow under this angle of attack is still attached and there is no need to utilize the leading-edge flow control array. Hence, the flow control is initially applied across the full trailing edge (channel and the wing), and, with an increase in C_μ, the base flow lift coefficient is increased to $C_L \approx 2.8$ at $C_\mu = 0.11$. However, the altered pressure about the circulation-controlled airfoil reaches a point at which any further increase in the flow control coefficient induces the leading-edge adverse pressure gradient that triggers the incipient flow separation even at $\alpha = 8°$. Flow separation along the leading edge would preclude further gains in C_L if (trailing-edge) C_μ were simply increased past the leading-edge flow separation point. For this reason, leading-edge flow control is added to the extent that further gain in C_L can be sustained. Naturally, there would be a need for more leading-edge flow control with further increase in the adverse pressure gradient, brought about by the further circulation control. Consequently, the increasing fraction of flow control input becomes used for the flow separation management, which alters the $\partial C_L/\partial C_\mu$ slope in the stall region, relative to the pre-stall circulation control. Hence, circulation control can be extended into the stall region, albeit at lower efficiency than in the pre-stall.

Since there is only one other example in the literature of channel wing circulation control along the channel trailing edge (Englar and Campbell, 2002), it is informative to compare the present channel circulation control results with that earlier study, which utilized a larger channel fraction of the wing (s_c/s = 0.44, compared to the present s_c/s = 0.35), and a continuous trailing-edge control jet along the channel end. A case for comparison is chosen such that both the present, discrete array of control jets and the continuous single-orifice jet of Englar and Campbell (2002) deliver the same C_μ/A_c = 0.072 relative to the channel planform area A_c, although the total C_μ, based on the wing planform area, was consequently higher for the prior study (C_μ = 0.032 vs. 0.025) due to the higher s_c. When the propellers were operated to deliver C_T = 0.6 in either study, the prop-generated lift coefficients were relatively close at C_L = 1.96 in the present work and C_L = 1.9 in the prior. Although the controlled lift coefficients do not differ much either, C_L = 2.25 and 2.28,

respectively, these results yield incremental changes $\Delta C_L = 0.29$ and 0.38, for the present and prior investigation. However, taking into account the corresponding fractions s_c/s for each study, the lift coefficient increments per unit channel scale are very similar in both studies, namely $\Delta C_L/(s_c/s) = 0.83$ and 0.86, respectively. Although the 'unit' effect of the present segmented and the prior continuous active flow control approaches appear to be very similar when compared at the same unit C_μ, it is noted that the same C_μ can be achieved at a smaller level of the dimensional flow control input – the mass flow rate (expressed through a different flow control parameter C_q), as shown in direct comparisons by Vukasinovic, Glezer and Funk (2023). In addition, the present study demonstrated successful implementation of the circulation control for the combination of the outboard wing section and the channel which had not been considered in earlier studies.

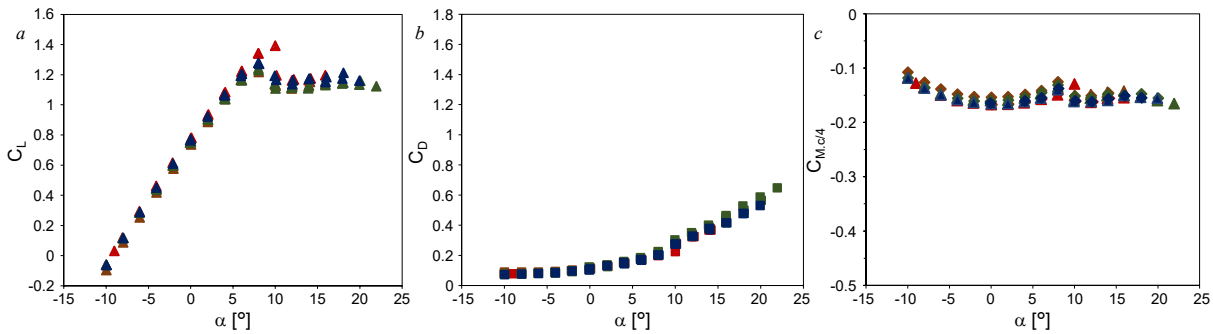

Figure 10. *Lift (a), drag (b), and pitch (c) coefficients with angle of attack for the airfoil model with installed inactive flow control modules at three free stream dynamic pressures q/q_c = 0.15 (green), 0.27 (brown), 0.31 (blue), and 0.43 (red).*

IV. Aerodynamic Bleed Control

As a reference to compare the effects of the various ADB configurations, baseline aerodynamic measurements are taken for dynamic pressures q/q_c = 0.15, 0.27, 0.31, and 0.43. The angle of attack is varied between -10° < α < 23°, while the flap remains permanently 'deployed' at θ = 70°, and all flow control modules are installed in the model but remain inactive. Figure 10 shows the resulting main aerodynamic load coefficient distributions. The lift curve is comparable to a non-channel wing, varying linearly with a slope of $\partial C_L/\partial\alpha \approx 0.08$, except that stall occurs as low as at $\alpha \sim 9°$. Consequently, the most interest in the flow control enhancement of aerodynamic lift will be placed at the angles of attack up to α = 8°, with lift coefficient $C_L \approx 1.3$ (Figure 10a). The corresponding drag curve (Figure 10b) indicates, as expected, a higher penalty in drag for a channel wing, compared to an equivalent non-channel wing,

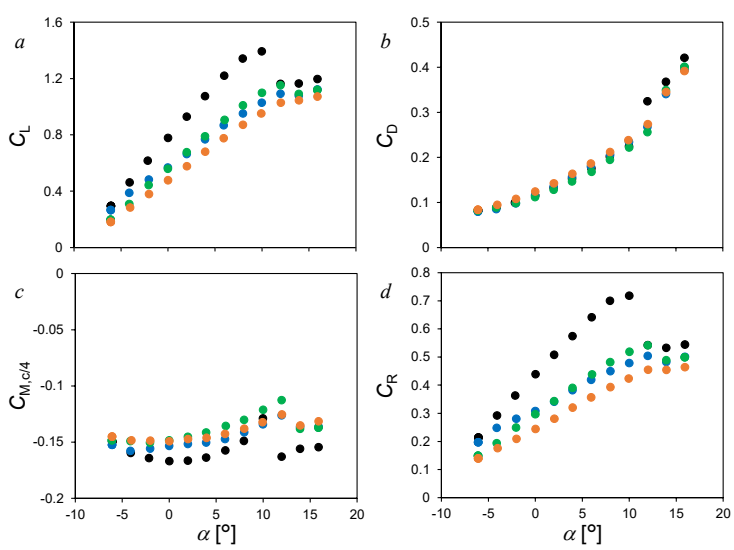

Figure 11. *Variation of C_L (a), C_D (b), $C_{M,c/4}$ (c) and C_R (d) with α ($Re_c = 5.8 \cdot 10^5$) for aerodynamic bleed from the forward segment (3.5% open area; ●), aft segment (3.5% open area; ●) and both segments combined (2.4% open area; ●), baseline (●).*

resulting in a pre-stall drag coefficient $C_D \approx 0.2$ and yielding a lift-to-drag ratio of ~6. Not shown are the corresponding distributions of the roll and yaw moments, as they are directly correlated with the lift and drag forces, and any changes in forces can be directly related to the changes in these moments. The pitching moment $C_{M,c/4}$ (Figure 10c) is negative (pitch-down) and increases slightly as α is increased, resulting in a weakly unstable condition because $\partial C_{M,c/4}/\partial\alpha > 0$. Interestingly, even in the stall condition, there is no appreciable difference in the pitching moment, except it being a slightly less variant with α.

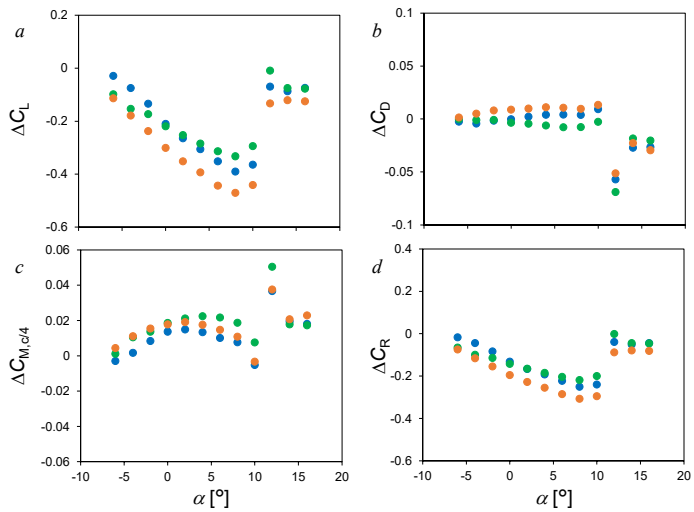

Figure 12. *Variation of ΔC_L (a), ΔC_D (b), $\Delta C_{M,c/4}$ (c) and ΔC_R (d) with α ($Re_c = 5.8{\cdot}10^5$) for baseline and aerodynamic bleed conditions. Symbols as in Figure 11.*

The effects of ADB are characterized by measuring the changes in aerodynamic loads in the presence of bleed flow from the two spanwise arrays of slots. Figure 11 shows the effect of varying the chordwise location of the bleed between the forward segment, aft segment and both segments combined (3.5%, 3.5% and 6.9% open area, respectively, on both *PS* and *SS*), along with the corresponding increments in Figure 12. The effect on lift (Figures 11a and 12a) of bleed from the forward segment (cf. Figure 1b) is negligible for $\alpha = -6°$ and increases with α, reaching $\Delta C_L = -0.36$ (26% decrease) for $\alpha = 10°$. Bleed from the aft segment leads to slightly reduced C_L for $\alpha < 0°$, but has less effect than bleed from the forward segment for $\alpha > 6°$, ostensibly due to the effects on the strength of the bleed flow resulting from changes in the pressure distribution around the surface as α is varied. Combining bleed from both segments leads to additional reduction in lift, up to $\Delta C_L = -0.44$ (32% decrease) for $\alpha = 10°$. At α above baseline stall ($\alpha > 10°$), where the flow over the *SS* becomes separated, the disturbance from the bleed has less effect on the surrounding flow, leading to a smaller reduction in lift ($\Delta C_L \sim -0.13$ using bleed from both segments). Bleed has a comparatively small effect on drag (Figures 11b and 12b) on the order of $\Delta C_D \sim \pm 0.02$ relative to baseline for $\alpha = 10°$ (i.e. below stall). At and above stall ($\alpha > 10°$), drag is

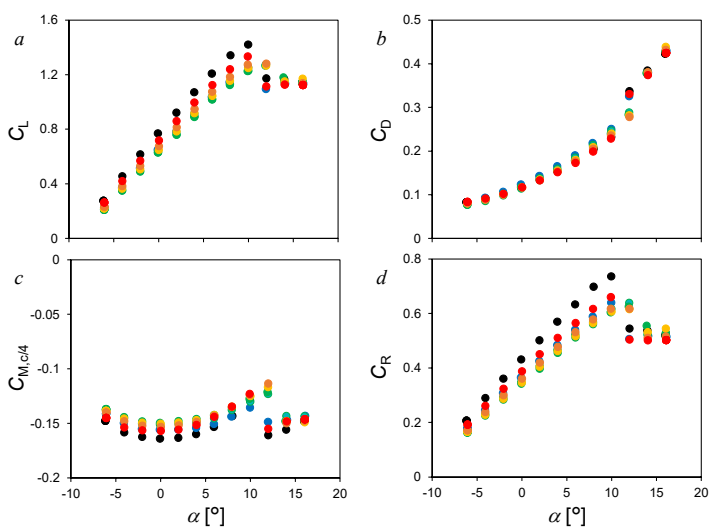

Figure 13. *Variation due to bleed of C_L (a), C_D (b), $C_{M,c/4}$ (c), C_R (d) with α (open area $\Phi = 1.2\%$): Spanwise position $s_b/s = 0.53$ (●), 0.62 (●), 0.70 (●), 0.79 (●), 0.87 (●), 0.96 (●).*

reduced, ostensibly to reduced lift-induced drag. In the absence of bleed, there is minimal variation in pitching moment with α (Figures 11c and 12c), indicating the aerodynamic center is near quarter-chord. In the presence of bleed, the pitching moment becomes less nose-down. The negative value ($C_{M,c/4} \sim -0.14$) is as expected for a wing with a negatively cambered airfoil. A significant rolling moment (Figures 11d and 12d) was also measured, varying according to trends comparable to the lift.

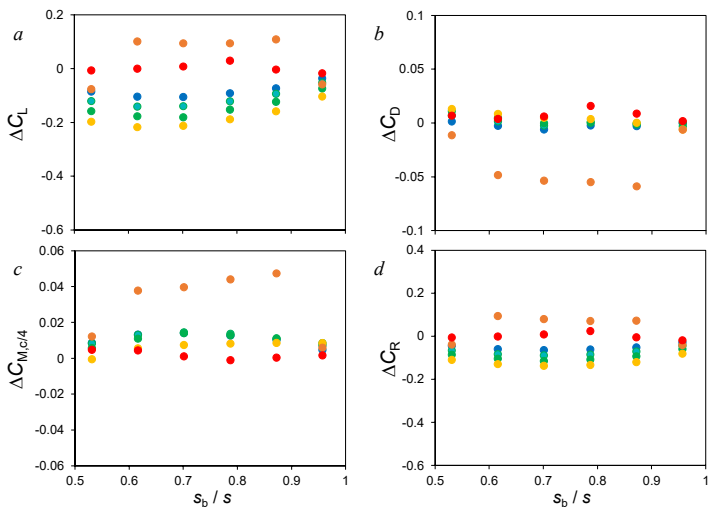

Figure 14. *Variation of ΔC_L relative to baseline (a), ΔC_D (b), $\Delta C_{M,c/4}$ (c) and ΔC_R (d) with spanwise position of bleed ports (Φ = 1.2%): α = -4 °(●), 0 °(●), 4 °(●), 8 °(●), 12 °(●), 16 °(●).*

Variation of the spanwise location of the bleed affects the aerodynamic loads (Figure 13), with the corresponding increments in Figure 14 shown as a function of the spanwise bleed port location. Across the full chordwise extent of the bleed area, spanwise segments of bleed openings with open area fraction Φ = 1.2% of the reference area are selectively opened on both the *SS* and *PS*. The reduction in lift (Figures 13a and 14a) for $\alpha < 12°$ increases with α as the pressure difference between the *PS* and *SS* increases, is smallest with bleed located at the outermost portion of the span ($s_b = 0.96s$) and increases as the bleed is moved spanwise inboard (toward the channel). For the innermost position ($s_b = 0.53s$) there is a slight reduction in the lift decrement, ostensibly due to interference from the channel and propeller strut. The corresponding change in drag (Figures 13b and 14b) is minimal, varying from $\Delta C_D = +0.02$ using bleed from the innermost position to nearly zero for bleed near the wingtip. For $\alpha = 12°$, i.e. near stall, bleed located at any spanwise location except the innermost and outermost position leads to an increase in lift of $\Delta C_L = +0.1$ and a change in drag of $\Delta C_D = -0.05$. These effects are conjectured to occur as a result of the bleed altering the spanwise loading distribution and tip vortex as discussed by DeSalvo et al. (2019), who show how as the tip vortex on a 3-D wing begins to break down as α is increased toward stall, the use of aerodynamic bleed near the

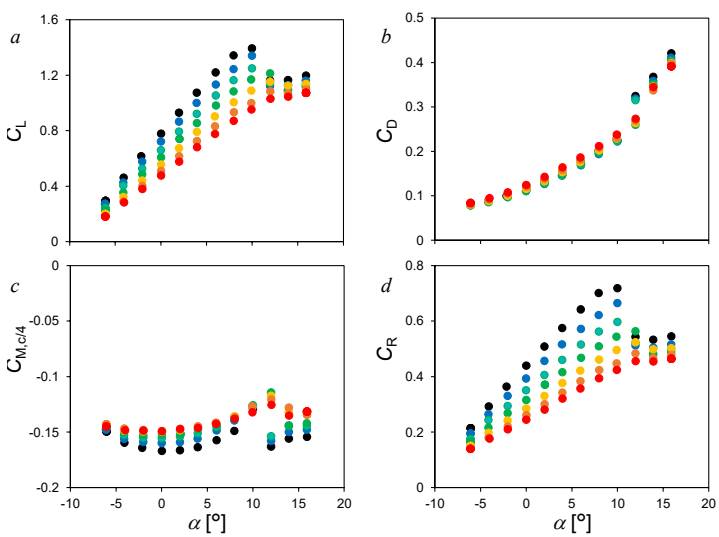

Figure 15. *Variation of C_L (a), C_D (b), $C_{M,c/4}$ (c) and C_R (d) with bleed open area fraction Φ (increasing from wingtip with additional open area toward root). Baseline (●), Φ = 1.2% (●), 2.3% (●), 3.5% (●), 4.6% (●), 5.8% (●), 6.9% (●).*

wingtip can cause streamwise vorticity near the tip to remain more organized, resulting in increased lift and reduced drag. As α is increased to 16° (above stall), bleed does not disturb the flow over the *SS*, and as a result there is no change in aerodynamic loads. The pitching moment (Figures 13c and 14c) becomes less nose-down, with minimal variation with α and a smaller change in the presence of bleed from near the wingtip (0.96*s*). The variation in C_R (Figures 13d and 14d) compares with the variation in C_L (Figures 13a and 14a).

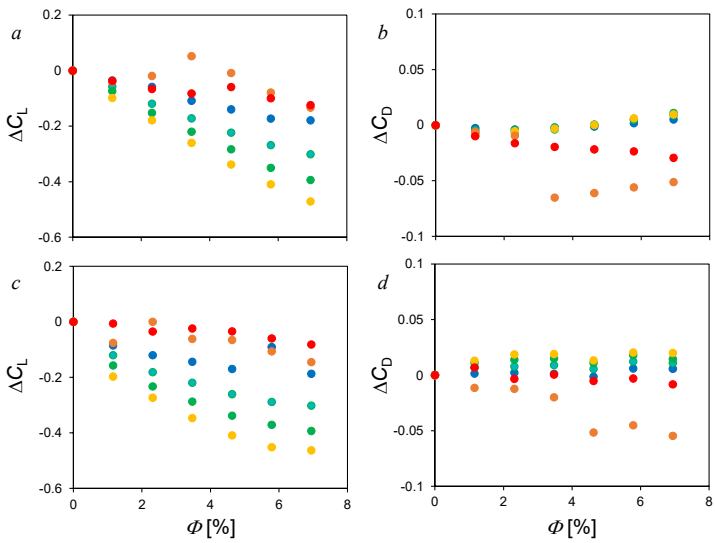

Figure 16. *Variation due to bleed of ΔC_L (a,b) and ΔC_D (c,d) relative to baseline with bleed open area fraction Φ. Bleed at wingtip (Φ increases with additional open area toward root; a,c), bleed at root (Φ increases toward tip; b, d). α = -4 °(●), 0 °(●), 4 °(●), 8 °(●), 12 °(●), 16 °(●).*

As the spanwise extent (and corresponding Φ) of the bleed is increased, the effect on the aerodynamic loads increases, as shown in Figure 15, where the bleed extent is increased inboard from the tip toward the root. For $\alpha < 12°$, i.e. below stall, the lift reduction increases linearly as Φ is increased (Figure 15a), while the drag varies only slightly (Figure 15b). At $\alpha = 12°$, i.e., near stall, the lift decrement decreases significantly as bleed can no longer disturb the flow over the *SS*. It is noteworthy that for $\Phi = 3.5\%$, where bleed is open across the outermost half of the outer span near the wingtip, there is a lift increase and a reduction in drag, as discussed in connection with Figure 14. Further increases in Φ, where additional bleed ports are opened near the root, result in lift decreasing while the drag reduction persists, suggesting that a sufficient spanwise extent of bleed near the tip may influence the tip vortex in a manner leading to reduced drag. As Φ is increased, $C_{M,c/4}$ (Figure 15c) becomes less nose-down, with the variation of $C_{M,c/4}$ with α decreasing as Φ is increased. The rolling moment (Figure 15d) varies proportionally to the lift, as discussed in connection with Figure 11d.

Shown in Figure 16 is a comparison between the effects of increasing the spanwise extent of the bleed inboard from the tip (Figures 16a,c) and outboard from the root of the outer span, i.e. the channel (Figures 16b,d). Below stall ($\alpha < 12°$), lift reduction increases monotonically with Φ for bleed extending inboard from the tip (Figure 16a; cf. Figure 15a). For bleed extending outboard from the root of the outer span (Figure 16b) the lift reduction is larger at lower Φ, because more lift is generated near the root than the tip, resulting in a larger effect from the bleed. In either instance, the lift reduction is greatly diminished for $\alpha \geq 12°$ upon the onset of stall. The changes in drag using bleed extending inboard from the tip (Figure 16c; cf. Figure 15b) are minimal for $\alpha < 12°$. As discussed in connection with Figure 14, a pronounced drag reduction is present at $\alpha = 12°$, i.e. near stall, as bleed near the outer span is increased, which is conjectured to occur as a result of the bleed flow altering the tip vortex. Likewise, using bleed near extending outboard from the root of the main wing, the drag increase is slightly higher ($\Delta C_D = 0.03$; Figure 16d), even

with bleed spanning as little as $\Phi = 2.3\%$, compared to bleed extending inboard from the tip, where a significant drag increase only occurs for $\Phi > 5\%$. For $\alpha = 12°$, i.e. near stall, the lift increase is reduced compared to lower α, and a reduction in drag comparable to that which occurs with bleed extending inboard from the tip (Figure 16b) is present. Above stall, only a slight reduction in drag as Φ is increased from either the tip or the main wing root.

VI. Conclusions

Enhanced aerodynamic performance of a channel wing model for improved short takeoff and landing (STOL) by enabling further reductions in critical takeoff speed and/or takeoff distance using fluidic based circulation control and distributed bleed actuation for improved maneuvering was assessed in low-speed wind tunnel investigations. While these investigations were primarily focused on pre-stall angles of attack, the effects of the actuation were also considered at the onset of stall. Circulation control for enhanced STOL characteristics was implemented using the Coanda effect by arrays of surface tangential fluidically-oscillating jet actuators along the trailing edges of both the channel and the outer wing segments. While over the trailing edge of the channel wing the Coanda surface was a half-cylinder, over the outer segment the Coanda surface was formed by an aggressive flap deflected at $\theta = 70°$. Aerodynamic distributed bleed (ADB) for enhanced aerodynamic maneuvering without a need for external moving control surfaces or pressurized air source was implemented across segmented skin panels on the pressure and suction sides of the outboard section of the wing.

While the use of the powered channel yields lift enhancement, the present investigations of the inactive channel showed that its integration also leads to an increase in drag and can induce stall at lower angles of attack. In the presence of the deployed flap, the lift curve is linear, with a slope of $\partial C_L/\partial\alpha \approx 0.08$, and stall was observed at $\alpha \approx 10°$. Based on the pre-stall ($\alpha = 8°$) lift and drag coefficients $C_L \approx 1.3$ and $C_D \approx 0.2$, the resulting lift-to-drag ratio is about 6.5. The quarter-chord pitching moment is largely invariant with α, with a value of $C_{M,c/4} \sim -0.16$ at $\alpha = 0°$, weakly increasing with the angle deflection away from zero angle of attack in the pre-stall region, while reaching up to 35% higher magnitude across the full measured span.

The aerodynamic loads can be varied by using distributed bleed actuation through openings in the surface of the outboard section of the wing. The flow through the bleed ports is driven through the interior of the wing by pressure differences in flight across the pressure and suction surfaces, and subsequently interacts with the surrounding flow to yield desired changes in the overall aerodynamic loads. Bleed near mid-chord on the outer span (6.9% of planform area) leads to lift decrements by up to $\Delta C_L = -0.44$ (32% of baseline). By establishing an "operating point" C_L below the baseline for a given angle of attack, the bleed can yield bi-directional direct lift control within a broad operating range encompassing both fully attached and stalled base flows. These aerodynamic loads can be varied without changing angle of attack in relation to the baseline airfoil by varying the streamwise and spanwise extent of the bleed flow, and by regulating the bleed flow using lightweight, low-power surface louvers.

Circulation control was assessed with both inactive and powered channel propeller at varying levels of the thrust coefficient C_T. While activating the propeller increases lift depending on the thrust and angle of attack, the present investigations primarily focused on the additional lift increment generated by the fluidic-based circulation control. Following benchtop development and characterization of actuators arrays over the trailing edges of the outer wing segment and of the channel, the jet arrays were integrated into the wind tunnel model and characterized in situ, in the absence of crossflow,

yielding the total thrust of the jets, which was used to determine the actuation's momentum coefficient C_μ. It was shown that the effects on the aerodynamic loads of the individual flow control arrays in the outer wing and channel are additive, yielding $\Delta C_L/\Delta C_D \approx 7 - 10$ at pre-stall angles of attack. In addition, at $\alpha = 8°$, with the propeller inactive, flow control reduces the required dynamic pressure at takeoff to 57% of what is needed in the absence of actuation. Activation of the propeller reduces the required dynamic pressure for takeoff by another 20%, and adding trailing-edge circulation control reduces the required dynamic pressure to only 45% of the base level. Alternatively, using the wing alone as a reference, the takeoff field length (TOFL) is reduced by 23.5% due to the powered-propeller effect in the channel, by 35% after the addition of active flow control in the channel, and by 50% after adding circulation control along the outer wing segment as well. Improvements in STOL characteristics were also demonstrated at incipient stall by using leading-edge actuation to promote flow reattachment over the suction surface, albeit with somewhat reduced efficiency or reduced $\partial C_L/\partial C_\mu$, compared to pre-stall circulation control.

Acknowledgment

This research was developed with funding from the Defense Advanced Research Projects Agency (DARPA) Control of Revolutionary Aircraft with Novel Effectors (CRANE) Program.

The views, opinions and/or findings expressed are those of the authors and should not be interpreted as representing the official views or policies of the Department of Defense or the U.S. Government.

The authors acknowledge GTRI Principal Research Engineer Burt Jennings and GT Research Engineer Dr. Svyatoslav Yorish for their assistance in the wind tunnel testing, particularly with respect to the wind tunnel model and auxiliary hardware design, assembly, shakedown, and operation.

References

Blick, E. F. and Homer, V., "Power-on Channel Wing Aerodynamics," *Journal of Aircraft*, Vol. **8** (4), pp. 234-238, 1971.

Custer, W., R., *Aeroplane*, US Patent #1,708,720, 1929.

Davidson, I. M., "The Jet Flap," *The Aeronautical Journal*, Vol. **60** (541), pp.25-50, 1956.

DeSalvo, M. and Glezer, A., "Aerodynamic Active Flow Control using Hybrid, Momentum-Based Actuation," *AIAA Paper* 2023-1991, 2023.

DeSalvo, M., Heathcote, D., Smith, M. and Glezer, A., "Direct Lift Control using Distributed Aerodynamic Bleed," *AIAA Paper* 2019-0591, 2019.

DeSalvo, M., Vukasinovic, B., Funk, R. and Glezer, A., "Hybrid AFC Actuation: Wind Tunnel Investigations," DARPA CRANE Symposium, April 2021.

Dimmock, N. A., "An Experimental Introduction to the Jet Flap," Aeronautical Research Council Technical Report C.P. No. 344, 1957.

Englar, R. and Campbell, B., "Development of Pneumatic Channel Wing Powered-lift Advanced SuperSTOL Aircraft," *AIAA Paper* 2002-2939, 2002.

Englar, R. J., "Application of Pneumatic Lift and Control Surface Technology to Advanced Transport Aircraft," in *Transportation Beyond 2000*, NASA, pp. 371-397, 1996.

Englar, R. J., "Circulation Control Pneumatic Aerodynamics: Blown Force and Moment Augmentation and Modification; Past, Present and Future," *AIAA Paper* 2000-2541, 2000.

Englar, R. J., "Overview of Circulation Control Pneumatic Aerodynamics: Blown Force and Moment Augmentation and Modification as Applied Primarily to Fixed-wing Aircraft," *NASA CP 2005-213509*, pp. 37-79, 2005.

Gunther, C., Marchman, J. and VanBlarcom, R., "Comparison of Channel Wing Theoretical and Experimental Performance," *AIAA Paper* 2000-0257, 2000.

Haus, F., "The Use of Slots for Increasing the Lift of Airplane Wings," NACA-TM-635, 1931.

Hu, T., Wang, Z. and Gursul, I., "Passive Control of Roll Oscillations of Low-Aspect-Ratio Wings using Bleed," *Experiments in Fluids*, Vol. **55**, No. 1752, 2014.

Keane, P.M. and Keane, A.J., "Use of Custer channel wings – Wing ducts on small UAVs," *Journal of Aerospace Engineering*, **29** (3), 04015059, 2016.

Kearney, J. M. and Glezer, A., "Aerodynamic Control of a Pitching Airfoil by Active Bleed," *AIAA Paper* 2014-2045, 2014.

Kearney, J. M. and Glezer, A., "Aero-Effected Control of a Pitching Airfoil by Bleed Actuation," *AIAA Paper* 2013-2519, 2013.

Kearney, J. M. and Glezer, A., "Aero-Effected Flight Control Using Distributed Active Bleed," *AIAA Paper* 2011-3099, 2011.

Kraushaar, S. and Chokani, N., "Afterbody Separation Control using Passive Porosity," *AIAA Paper* 1997-3003, 1997.

Lachmann, G., "Results of Experiments with Slotted Wings," NACA TN 282, 1924.

Mihalik, J. and Keane, A.J., "Custer Channel Wings for Short Takeoff and Landing of Unmanned Aircraft," *Journal of Aircraft*, **59** (1), pp.196-205, 2022.

Oshima, E. K., Gharib, M., Reichert, J., and Wygnanski, I. J., "On the Use of Power-Based Parameters for Blowing Active Flow Control Systems," *AIAA Journal* **61** (3), pp. 1-12, 2023.

Pasamanick, J., "Langley Full-scale-tunnel Tests of the Custer Channel Wing Airplane," *NACA-RM-L53A09*, 1953.

Tanner, M., "Reduction of Base Drag," *Progress in Aerospace Sciences*, Vol. **16** (4), pp. 369-384, 1975.

Vukasinovic, B., Glezer, A., and Funk, R.B., "DARPA CRANE Circulation Control using Arrays of Discrete Fluidic Actuator Jets," *AIAA Paper* 2023-1992, 2023.

Williams, J., Butler, S.F.J. and Wood, M.N., "The Aerodynamics of Jet Flaps," *Aeronautical Research Council*, R&M No. 3304, 1961.

Zilberman, M., Haber, Y., Azarzar, M., and Kamins, M., "Custer Channel Wing (CCW) Phase III," *AIAA Paper* 2021-0113, 2021.